

On the origin of microstructural discontinuities in sliding contacts: a discrete dislocation plasticity analysis

Y. Xu^{1,2}, F. Ruebeling^{3,4}, D.S. Balint¹, C. Greiner^{3,4}, D. Dini^{1*}

¹ Department of Mechanical Engineering, Imperial College London, South Kensington Campus, Exhibition Road, London SW7 2AZ, UK

² Department of Materials, Imperial College London, South Kensington Campus, Exhibition Road, London SW7 2AZ, UK

³ Karlsruhe Institute of Technology (KIT), Institute for Applied Materials (IAM), Kaiserstrasse 12, 76131 Karlsruhe, Germany

⁴ KIT IAM-CMS MicroTribology Center (μ TC), Strasse am Forum 5, 76131 Karlsruhe, Germany

Abstract

Two-dimensional discrete dislocation plasticity (DDP) calculations that simulate single crystal films bonded to a rigid substrate under sliding by a rigid sinusoid-shaped asperity are performed with various contact sizes. The contact between the thin film and the asperity is established by a preceding indentation and modelled using a cohesive zone method (CZM), whose behavior is governed by a traction-displacement relation. The emergence of microstructural changes observed in sliding tests has been interpreted as a localized lattice rotation band given rise by the dislocation activities underneath the contact. The depth of the lattice rotation band is predicted to be well commensurate with that observed in the corresponding tests. Furthermore, the dimension and magnitude of the lattice rotation band have been linked to the sliding distance and contact size. This research reveals the underpinning mechanisms for the microstructural

*Corresponding Author: Prof. Daniele Dini, Email: d.dini@imperial.ac.uk

1 changes observed in the sliding tests by explicitly modelling the dislocation patterns
2 and highly localized plastic deformation of materials under various indentation and
3 sliding scenarios.

4 **Keywords:** Sliding; Discrete Dislocation Plasticity; Lattice rotation; Size effect

1 **1 Introduction**

2 Microstructure determines the material performance under contact, including but not
3 limited to hardness (Chenje et al., 2004), coefficient of friction (COF) (Rigney and
4 Hirth, 1979), anti-fretting (Zhang et al., 2009) and wear resistance (Rigney and Glaeser,
5 1978) under a tribological loading condition, particularly when the contact size
6 approaches the grain size. Correspondingly, the subsurface microstructure of specimens
7 is simultaneously changed by the plasticity induced by external tribological load that
8 couples normal and tangential components. Therefore, it is significant to understand the
9 mechanisms of the mutual interactions between the microstructure and the local
10 deformation of materials under tribology loadings. Among complex tribology loading
11 scenarios, the single asperity sliding problem provides an elementary mechanistic
12 benchmark for revealing the mechanisms for microstructure change.

13 The phenomenon of microstructure variation in the sample subsurface under
14 tribological loads has commonly been observed in experimental studies *e.g.* (Hattori et
15 al., 2008; Hughes and Hansen, 2001; Stoyanov et al., 2014) on various crystalline
16 metals, including nickel, copper and aluminum. Numerical investigations including the
17 work (Karthikeyan et al., 2009; Pastewka et al., 2011) were performed to understand
18 the intrinsic mechanisms of the subsurface modification under sliding. However, due
19 to the complexity of the tribology contact loads, neither of the experimental nor
20 numerical studies have not yet elucidated the phenomenon with satisfactory
21 mechanisms. A more recent experimental study (Greiner et al., 2016) using Scanning
22 Transmission Electron Microscopy (STEM) has shown a “dislocation traceline”, *i.e.* an
23 apparent contrast change in the STEM images within the subsurface of a copper
24 specimen after one-stroke sliding. The abrupt contrast change was interpreted as a

1 special dislocation piling up pattern under the contact and serves as a key mechanistic
2 driver giving rise to subgrain boundary formation and further damage in subsequent
3 cyclic tribological loading (Greiner et al., 2016).

4 There are no physics-based mechanisms that have yet been proposed to provide a
5 convincing insight for the emergence of tracelines observed in sliding tests. In order to
6 interpret microstructural changes observed in the subsurface during sliding tests, a
7 previous study (Greiner et al., 2018) employed a continuum model to describe the
8 dislocation activity by assessing the inhomogeneous stress field variation under the
9 moving indenter. However, due to the lack of a length scale parameter and the discrete
10 nature of the phenomenon under investigation, neither conventional continuum
11 approaches nor crystal plasticity (*e.g.* Dunne et al. (2007b)) is capable of capturing the
12 highly localized and discrete deformation observed in the experiments. It is in fact more
13 sensible to explicitly model dislocation activities that appear to be likely responsible
14 for the microstructural discontinuities. Hence, a 2D Discrete Dislocation Plasticity
15 (DDP) model is established in this paper to simulate the evolution of dislocations
16 motion and their pile up pattern under the sliding. The DDP numerical framework has
17 been extensively applied to provide microstructure- and length-scale associated
18 interpretation to a variety of fundamental micromechanical problems, including tension
19 (Balint et al., 2008), micro-compression (Akarapu et al., 2010), bending (Prastiti et al.,
20 2020; Tarleton et al., 2015), nano-indentation (Qu et al., 2006) and pure sliding
21 (Deshpande et al., 2004) by simulating the activity of individual dislocations that is
22 governed by nucleation, mobility and pinning laws. In this framework, the material
23 behavior is completely determined by the collective activities of dislocations under
24 contact. The contact between the specimen and indenter that is established by a
25 preceding sinusoidal micro-indentation is modelled using a cohesive zone method

1 (CZM), whose shear stress performance is governed by a non-soften traction-
2 displacement relation (Deshpande et al., 2007). We herein aim to investigate the
3 underpinning mechanisms for local microstructural deformation and the induced lattice
4 rotation under single asperity sliding using the DDP framework integrated with
5 experimental observation (Ruebeling et al., 2020). The numerical results shed light on
6 the mechanisms for the emergence of the dislocation tracelines observed in the
7 experiment by explicitly illustrating the dislocation piling up, geometrically necessary
8 dislocations (GND) and consequently localized lattice rotation of the subsurface under
9 various indentation and sliding scenarios. In addition, this research also provides a
10 pioneering framework for simulating the localized deformation and the subsequent
11 microstructure changes observed in the multi-cycle tribological tests, *e.g.* shown in the
12 work (Greiner et al., 2016). The results of the analysis also benefit researchers and
13 engineers in their pursuit of tailored and optimized the anti-wear properties of materials
14 and coatings.

15 **2 Methodology**

16 **2.1 Discrete Dislocation Plasticity formulation**

17 We use the classical 2D plane strain, isotropic discrete dislocation plasticity (DDP)
18 computational framework first described by Van der Giessen and Needleman (Van der
19 Giessen and Needleman, 1995). This DDP framework explicitly simulates the
20 nucleation, glide and interaction of the purely edge parts of individual dislocation loops
21 in single and polycrystal geometries subject to boundary conditions and a plane strain
22 constraint. The formulation exploits Bueckner's principle to represent the collective
23 effect of dislocations by their linear elastic superposition; plasticity arises from the
24 irreversible, quasi-static evolution of the positions of the elastic fields of all dislocations

1 in the system. The essential details of the DDP framework are given in (Balint et al.,
2 2005; Xu et al., 2020); only the aspects of the DDP formulation that are distinct from
3 the basic recipe are described here.

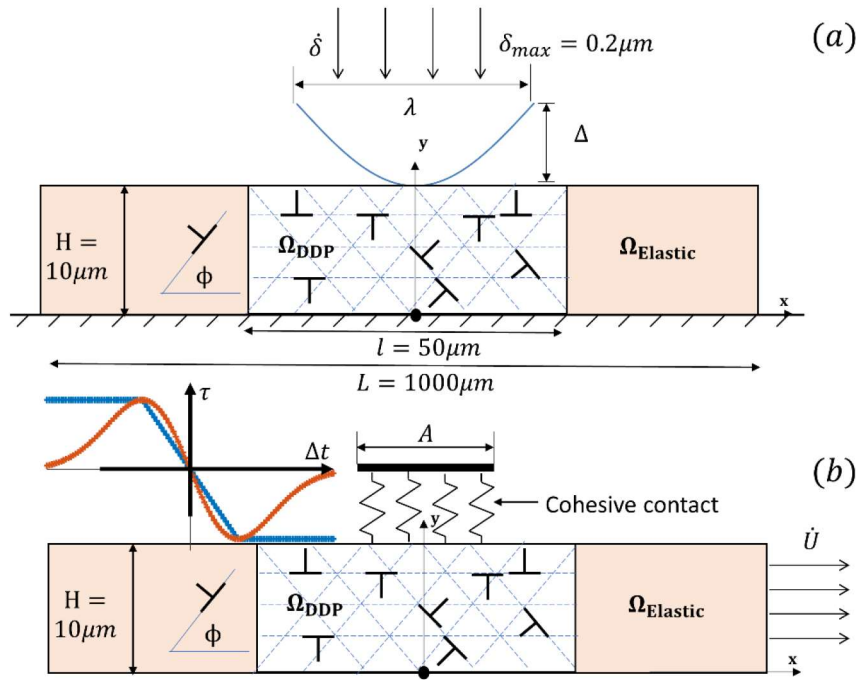
4 **2.2 The DDP model setup for sliding**

5 The basic DDP model described above is adapted here for frictional sliding problems.
6 The aim is to use the model to reproduce the experimental observation, hence enable
7 its physical interpretation. An initial sinusoidal indentation process is utilized to
8 establish contact between the rigid asperity and the specimen. This is followed by
9 monotonic sliding with a cohesive zone model (CZM) between the asperity and the
10 specimen (Deshpande et al., 2004).

11 The specimen is made of a DDP region underneath a sinusoidal asperity with an elastic
12 medium on either side, as depicted in **Figure 1**. The DDP *process window* represents a
13 single FCC-like crystal in a plane strain orientation and is assigned with aluminum-like
14 properties. Further details of the DDP parameters associated with this crystal
15 representation can be found in Xu et al. (2016). Although the crystal representation does
16 not correspond exactly to the pure copper tested in the experiments, the similarity of
17 the slip systems ($\Phi^{(\alpha)} = 0, \pm 45^\circ$ with respect to the x -axis in the model) to those in the
18 experiments enables mechanistic study of the microstructural change observed in the
19 sliding tests.

20 The DDP process window with dimension $l \times h$ is discretized by a finite element mesh
21 (the finite element method is used to solve the correction, or reduced problem of the
22 Bueckner linear superposition) that is highly focused towards the centre of the contact
23 area. The finite element mesh is made up of 240×100 bi-linear elements with a typical
24 mesh size of $\Delta x = 0.005 \mu\text{m}$ in the refined zone, which has dimensions $1 \mu\text{m} \times 1 \mu\text{m}$.

1 A mesh-size sensitivity study was conducted, and the mesh size mentioned above was
 2 found to be an optimal balance between computation expense and numerical accuracy.
 3 A sufficiently-small time increment of $\Delta t = 0.5\text{ns}$ was used to sufficiently resolve the
 4 evolution of the dislocation structure.



5
 6 **Figure 1.** Schematic illustration of (a) the sinusoidal indentation and (b) the subsequent
 7 monotonic sliding boundary value problem, solved using the DDP model.

8 Although the sinusoidal indentation model invokes a small strain approximation, the
 9 contact between the indenter and film is based upon the *deformed* film surface.
 10 Indentation depth is denoted by δ , and true contact length A is defined as the distance
 11 between the intersections of the indenter surface and the deformed film surface. In
 12 general, the true contact length A differs from the nominal contact length as material
 13 sink-in or pile-up (Balint et al., 2006) occurs. Also, nominal contact area does not
 14 account for the effect of surface roughness, comprised of steps created by dislocations
 15 exiting at the free surface, on the contact area, hence hardness (as analyzed and
 16 discussed in Widjaja et al. (2007)a.

1 The total reaction force of the thin film response to the applied indentation depth is
 2 computed as in eq. (1):

$$F = - \int_{-A/2}^{A/2} T_y(x, H) dx \quad (1)$$

3 where T_y is the surface traction in the y -direction, hence the indentation pressure (*i.e.*
 4 instantaneous or indentation depth-dependent hardness) p is defined by:

$$p \equiv F/A \quad (2)$$

5 where A is the actual, end-to-end length definition of the contact area.

6 The interaction between surfaces can be modelled by applying a continuum cohesive
 7 formula (Johnson, 1997). In the sliding simulations, the interaction between the
 8 sinusoidal asperity and the specimen is modelled using a cohesive zone on the
 9 contacting surface of length A with a relation between shear traction versus
 10 displacement, which is given by:

$$T_t = \begin{cases} -\tau_{max} \frac{\Delta t}{\delta_t}, & \text{if } |\Delta t| < \delta_t \\ -\tau_{max} \text{sign}(\Delta t), & \text{if } |\Delta t| > \delta_t \end{cases} \quad (3)$$

11 where $\Delta t = u_x(x, H)$ is the tangential displacement jump across the cohesive surface,
 12 and $T_t = T_x$ is the shear traction. Hence the interaction is a cohesive resistance to the
 13 relative sliding of the thin film. Traction free boundary conditions are applied on the
 14 part of the surface outside of the contact region:

$$T_x = T_y = 0 \text{ on } x = 0 \notin S_{contact} \text{ and } y = H \quad (4)$$

15 The maximum cohesive strength τ_{max} is set to be $\tau_{max} = 300\text{MPa}$ and the threshold
 16 displacement jump is $\delta_t = 0.5 \text{ nm}$. The parameter values in the non-softening traction-
 17 displacement relation are identical to Deshpande et al. (2007).

1 The displacement rates,

$$\dot{U}_x = \dot{U}, \dot{U}_y = 0 \quad (5)$$

2 are imposed on the specimen boundaries $x = \pm L/2$, and $y = 0$, to simulate the relative
3 sliding of the specimen with respect to the contact surface with magnitude $\dot{U}/A =$
4 10^4s^{-1} in the positive x -direction. The maximum sliding distance is set as
5 approximately one half of the corresponding contact size A , which is sufficiently large
6 to achieve a full slip condition (see the later discussion in Section 3.2) of the film. The
7 sliding rate \dot{U} was chosen sufficiently low to ensure a quasi-static sliding process, *i.e.*
8 that dislocations are in an equilibrium configuration at any sliding instance, hence the
9 effect of loading rate on sliding (due to nucleation time and mobility as shown in Song
10 et al., 2016) is negligible. The averaged shear stress τ along the contact is given by:

$$\tau = -\frac{1}{A} \int_{-A/2}^{A/2} T_x(x, H) dx \quad (6)$$

11 Different from the pure sliding calculations where films are assigned with a dislocation-
12 and stress-free initial state using the DDP framework, *e.g.* Benzerga (2008), the sliding
13 simulations herein start with a certain normal load and actual contact size to
14 accommodate the experimental setup. In fact, this type of sliding calculation is initiated
15 with a deformation field and dislocation structure in the specimen that is introduced
16 from the initial sinusoidal indentation simulations described above, with varying
17 indentation depth.

18 **2.3 Lattice rotation calculation**

19 We use the DDP framework described above to model the microstructural change, more
20 specifically, the elastic lattice rotation within the thin film under frictional sliding

1 scenarios. The lattice rotation is defined as the antisymmetric part of the displacement
 2 gradient tensor, which for the planar situation can be expressed in terms of the off-
 3 diagonal components of the small strain tensor ϵ_{ij} as:

$$\Omega = \frac{1}{2}(\epsilon_{21} - \epsilon_{12}) \quad (7)$$

4 where the small strain tensor is given by:

$$\epsilon_{ij} = \frac{1}{2} \left(\frac{\partial u_i}{\partial x_j} + \frac{\partial u_j}{\partial x_i} \right) \quad (8)$$

5 Lattice rotation is comprised of the derivatives of the displacements in the infinite plane
 6 discrete dislocation field and ($\tilde{}$) and the continuum correction field ($\hat{}$):

$$\Omega = \frac{1}{2}(\hat{u}_{2,1} + \tilde{u}_{2,1} - \hat{u}_{1,2} - \tilde{u}_{1,2}) \quad (9)$$

7 The DDP model considers only glide of edge type dislocations along predefined slip
 8 systems within the material, which introduce slip (displacement discontinuities) across
 9 the slip planes. A cluster of dislocations piling up introduces lattice rotation to the
 10 material. This phenomenon has also been reported in indentation problems (Balint et
 11 al., 2006; Po et al., 2019; Zhang et al., 2014). Displacement discontinuities should not
 12 appear in the derivatives of the displacements, they are continuous, however this
 13 requires analytical differentiation. Standard numerical differentiation of the dislocation
 14 displacement fields will reveal a discontinuity, a fact that is often exploited for
 15 visualization of slip localization (Hirth and Lothe, 1982). Hence when computed in this
 16 way, the definition of lattice rotation Ω in eq. (9) naturally excludes slip features from
 17 the ($\tilde{}$) field

18 In principle, we can employ a different background mesh, using interpolation, that is
 19 different from the finite element mesh used in the calculation in order to change the

1 resolution of field quantities. In this work we resolve field quantities on the highly
2 focused mesh used in the simulation to maintain their spatial resolution in the vicinity
3 of the indentation, especially near the contact surface. The lattice rotation calculation
4 was performed every 100 times increments, i.e. $\Delta U/A = 5 \times 10^{-4}$, to capture the
5 temporal evolution of lattice rotation against sliding distance.

6 The aforementioned elastic lattice rotation method was verified for a wedge-shaped
7 indentation problem; a comparison to prior simulations (such as Zhang et al. (2014)) is
8 shown in the [Appendix](#). The abrupt change in the sign of the lattice rotation near the
9 midline of the contact is consistent with experimental observations (Kysar et al., 2010)
10 and continuum plasticity analyses (Bouvier and Needleman, 2006). The values of lattice
11 rotation predicted here are also consistent with Zhang et al. (2014). It is worth noting
12 that the lattice rotation distribution is obtained by the combined effect (linear
13 superposition of fields) of dislocations on the three slip systems, and the lattice rotation
14 caused by isolated dislocations is long range. Therefore, the lattice rotation distribution
15 shows a different pattern from the corresponding dislocation distribution, since the
16 rotations caused by isolated, moving dislocations is experienced far from the
17 dislocations themselves; in other words, regions with a high value of dislocation density
18 do not necessarily exhibit a hot spot of lattice rotation. This phenomenon is further
19 illustrated and discussed when looking at the evolution of lattice rotation contours and
20 dislocation structure in the following sections (see *e.g.* **Figure 9**).

21 **3 Numerical results**

22 **3.1 Sinusoidal indentation response**

23 The variation of actual indentation pressure p_A and actual indentation contact area A
24 against applied indentation depth δ under the rigid sinusoidal asperity with an

1 amplitude $\Delta = 0.5\mu\text{m}$ and wavelength $\lambda = 10\mu\text{m}$ are reported in **Figure 2**. The
2 indentation pressure does not exhibit a strong indentation size effect (ISE) response,
3 consistent with micro-indentation tests (Kuksenko et al., 2019; Pharr et al., 2010) and
4 numerical simulations (Balint et al., 2006; Lewandowski and Stupkiewicz, 2018;
5 Saraev and Miller, 2006), when the indentation depth exceeds $\delta = 0.02\mu\text{m}$. The
6 presence of an ISE requires a high strain gradient in the plastically deforming volume
7 under the indenter (Nix and Gao, 1998), accommodated by a high density of
8 geometrical necessary dislocations (GNDs). However, the relatively blunt, smooth
9 surface of the sinusoidal indenter (e.g. compared to a wedge) used here suppresses the
10 development of the strain gradient when indentation depth is sufficiently large ($\delta >$
11 $0.02\mu\text{m}$), and the actual indentation pressure response stabilizes at a plateau level that
12 represents the continuum hardness of the specimen. The hardness value predicted here,
13 $p_A \cong 210\text{MPa}$, is reasonably close to the continuum plasticity prediction, $p_A = 3\sigma_Y$,
14 which establishes that plastic flow dominates the specimen response under sinusoidal
15 indentation with a large contact size. The size-insensitive indentation pressure regime
16 is useful in understanding the shear stress response in later sliding calculations by
17 excluding the normal stress interference. Compared to the nominal contact size (dashed
18 line in **Figure 2**), the actual contact size systematically exhibits a smaller value by
19 virtue of the material sink-in near the contact, which was observed in prior DDP
20 analyses of indentation (Widjaja et al., 2007b; Xu et al., 2019).

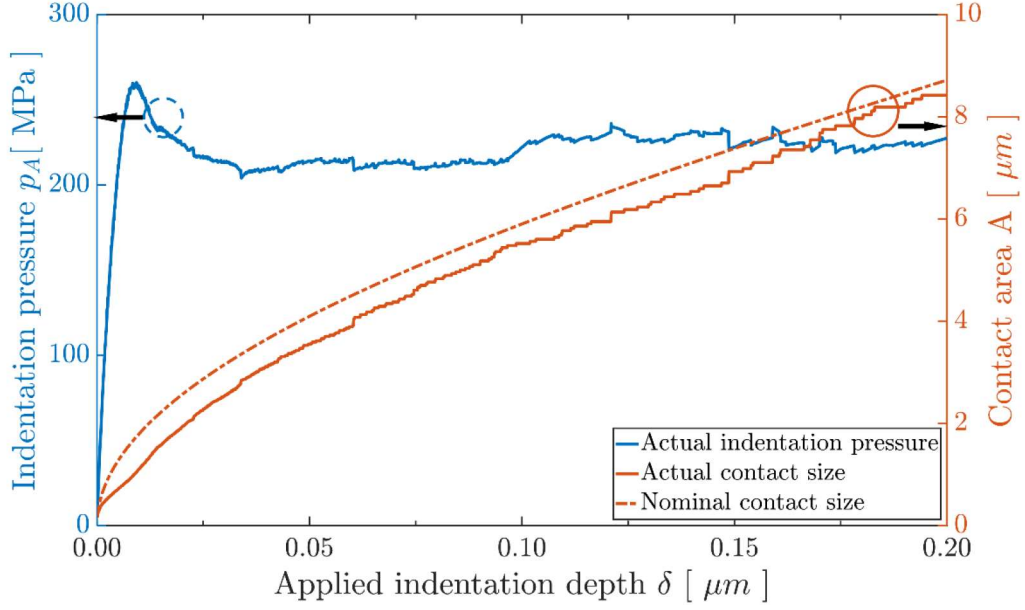


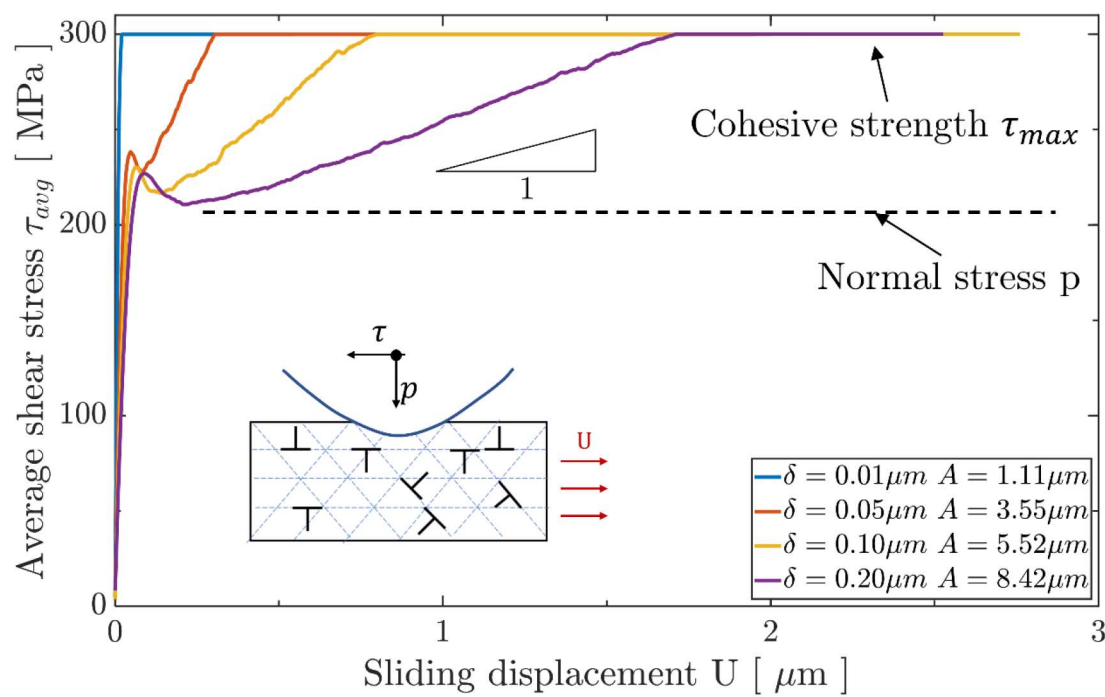
Figure 2. Actual indentation pressure p_A and actual contact size A versus applied indentation depth δ by the sinusoidal asperity with $\lambda = 10\mu\text{m}$ and $\Delta = 0.5\mu\text{m}$. The nominal contact size A_N (denoted by the dash-dot line) response is also included for comparison.

3.2 Subsurface deformation at different stages during sliding

The evolution of the average shear stress τ_{avg} along the contact with the sliding distance U is reported in **Figure 3** using the DDP model. The results were obtained from sliding simulations starting from four different initial indentation depths, $\delta = 0.01, 0.05, 0.10, 0.20\mu\text{m}$, with a sinusoidal asperity shape with $\lambda = 10\mu\text{m}$ and $\Delta = 0.5\mu\text{m}$, and the corresponding actual contact sizes $A = 1.11, 3.55, 5.52, 8.42\mu\text{m}$, respectively, were achieved by the initial indentation. Following an initial linear response, the evolution curves continue to increase but with a much slower and strongly contact size dominated rate $\partial\tau/\partial A$ until the cohesive strength τ_{max} is achieved. It can be observed that the critical sliding distance for the average shear stress achieving the cohesive strength depends on the contact size. In previous studies on sliding calculations without a prior indentation, the shear stress was found to be inversely square root dependent on the contact size (Deshpande et al., 2007). The preceding

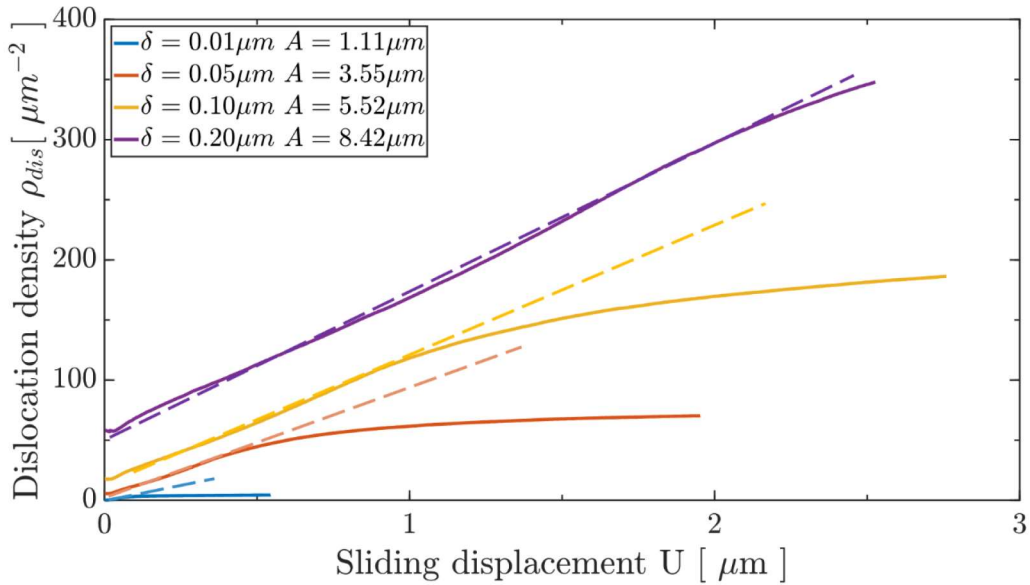
1 sinusoidal indentation in this research introduces considerable plasticity into the film
 2 prior to the sliding, therefore the relationship revealed under pure sliding does not hold
 3 when indentation is first applied. The quantitative relation between the shear stress
 4 increase with the initial indentation and the contact size will be investigated in detail in
 5 future studies.

6 The total dislocation density ρ_{dis} (number of dislocations divided by the area of the
 7 dislocation process window) evolution with the sliding distance U is reported in **Figure**
 8 **4**, where results were obtained from the aforementioned DDP simulations for four
 9 difference contact sizes. The total dislocation density linearly increases from a base
 10 value that was inherited from the preceding indentation. The rate of increase in the
 11 dislocation density is found to be independent of contact size.



12
 13 **Figure 3.** Shear stress τ evolution with sliding displacement U for four different
 14 contact sizes that are introduced by initial sinusoidal indentation. The normal stress p
 15 and cohesive strength τ_{max} are denoted for reference.

1 After a critical sliding distance, the rate of increase is reduced for all contact sizes, when
 2 more plasticity is introduced into the specimen by virtue of the increased sliding load;
 3 the critical sliding distance at which this occurs strongly depends on the contact size,
 4 and is greater than the critical sliding distance at which the average shear stress achieves
 5 the cohesive strength for a given contact size (see **Figure 3**). For instance, the critical
 6 sliding distances are predicted as $1.0\mu\text{m}$ and $0.76\mu\text{m}$ for the dislocation density
 7 evolution and shear stress evolution, respectively, for a contact size $A = 5.52\mu\text{m}$. The
 8 dislocation density eventually reaches a plateau value (except for the largest contact
 9 size $A = 8.42\mu\text{m}$), which is determined by the contact size, and ceases to increase with
 10 sliding distance. This suggests that the film is saturated by a stable dislocation structure,
 11 therefore full slip between the contact and specimen occurs.



12

13 **Figure 4.** Total dislocation density ρ_{dis} evolution against sliding displacement U under
 14 different contact sizes introduced by an initial sinusoidal indentation. The dashed lines
 15 indicate the contact-size independent dislocation density increase rate prior to full slip
 16 occurring.

17 Hence, three different sliding stages are identified, demarcated by the two
 18 aforementioned critical sliding distances for a given contact size. While the average
 19 shear stress evolution reflects plastic flow due to dislocation activity within the surface

1 region (Deshpande et al., 2004, 2005) only, the dislocation density evolution is able to
2 identify the point at which the full slip state initiates, *i.e.* when the dislocation structure
3 and deformation field within the entire specimen reach a dynamic equilibrium and the
4 dislocation density tends to saturate as sliding takes place. In the following sections,
5 lattice rotation maps in the whole specimen are analyzed at different sliding stages for
6 various contact sizes.

7 **3.3 Lattice rotation evolution during sliding**

8 The lattice rotation is calculated using eq. (9) according to the dislocation structure and
9 deformation field at a certain instant of a sliding process. The evolution of the lattice
10 rotation distribution for the contact size $A = 3.55 \mu\text{m}$ for single-stroke (left to right)
11 sliding is illustrated in **Figure 5** with individual dislocations shown explicitly as black
12 marks; a view of the entire specimen is shown above a close-up view of the
13 $10\mu\text{m} \times 1\mu\text{m}$ dashed region shown. With increase in sliding distance the lattice
14 rotation accumulates underneath and behind the contact. In particular, it is shown that
15 the lattice rotation introduced by the indentation that precedes sliding is negligible
16 compared to that induced by the sliding itself. As shown in (c) and (d), after sufficient
17 sliding the lattice rotation in a thin layer of material immediately underneath the contact
18 with thickness $h^* \approx 100 \text{ nm}$ has its lattice rotation ‘locked in’, *i.e.* it does not increase
19 in intensity but does spread with further sliding.

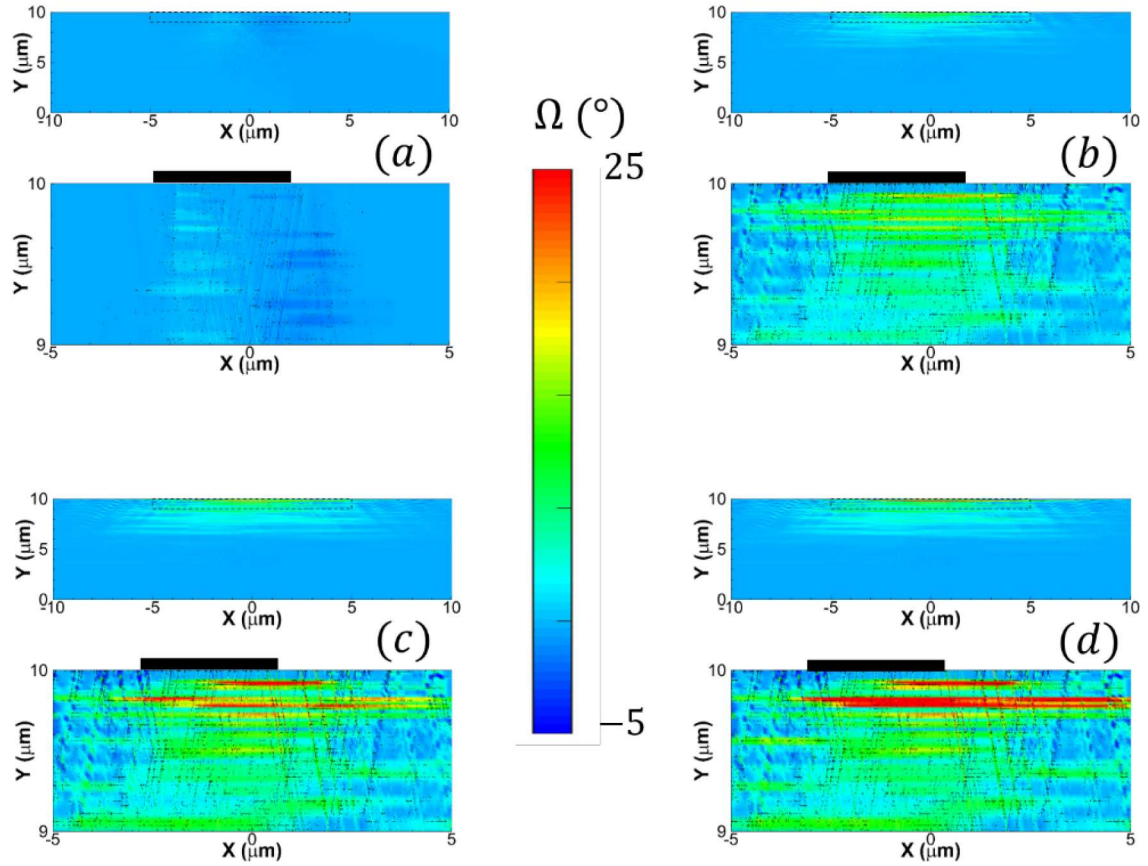


Figure 5. The contours of lattice rotation Ω and the corresponding dislocation structures (individual dislocations represented as black dots) of the sliding calculation starting from $\delta = 0.05 \mu\text{m}$ and $A = 3.55 \mu\text{m}$. Results are shown for sliding distances (a) $U = 0$ (i.e. just after indentation), (b) $U = 0.497 \mu\text{m}$ (the initial slip), (c) $U = 1.561 \mu\text{m}$ (partial slip) and (d) $U = 1.953 \mu\text{m}$ (full sliding), where U is the relative surface displacement, A the contact size and δ the indentation depth. The set of lattice rotation contours with corresponding dislocation structures illustrate the emergence of the ‘locked-in’ and localized lattice rotation bands during the sliding process.

This is accompanied by localization of lattice rotation in a thin band beneath this layer, which spreads parallel to the sliding direction and increases in strength as the sliding distance increases. More bands of localized lattice rotation with associated ‘locked-in’ layers are visible with increasing distance below the surface, particularly once the full sliding conditions are achieved (**Figure 5(d)**). The ‘locked-in’ lattice rotation bands correspond to the trace lines experimentally observed in Greiner et al. (2016), Greiner et al. (2018), where the localization band is the boundary between them.

1 Lattice rotation within a single crystal material is associated with the presence of
2 geometrically necessary dislocations (GNDs) (Arsenlis and Parks, 1999),
3 microstructure change (Cheng and Ghosh, 2015; Cheong et al., 2005; Das et al., 2018;
4 Dunne et al., 2007a) and non-local effect (Counts et al., 2008; Meissonnier et al., 2001).

5 The results shown in the following sections correspond to sliding distances that exceed
6 that required for the full sliding condition, beyond which the layered lattice rotation
7 distribution depicted in **Figure 5** is fully developed.

8 **3.4 Contact size effect on lattice rotation**

9 The contact size plays a crucial role (Deshpande et al., 2007; Liu et al., 2018) as it
10 strongly affects the plasticity introduced into the specimen. Besides the shear stress and
11 dislocation density reported in previous sections, the localized lattice rotation band and
12 the ‘locked-in’ layer, henceforth referred to as a trace line to be consistent with the
13 experiments, are illustrated for different contact sizes in **Figure 6**. As expected, a larger
14 contact size produces a dislocation structure with a larger number of dislocations, which
15 propagate much deeper into the indented material; this is also associated with the
16 formation of more than one trace line. However, the location and intensity of the trace
17 lines is nearly independent of the contact size, at least for smaller contact sizes, which
18 correspond to smaller loads in the experiments. Of more significance, the depth from
19 the surface of the first trace line is also independent of the contact size. This is consistent
20 with experiments (Greiner et al., 2016).

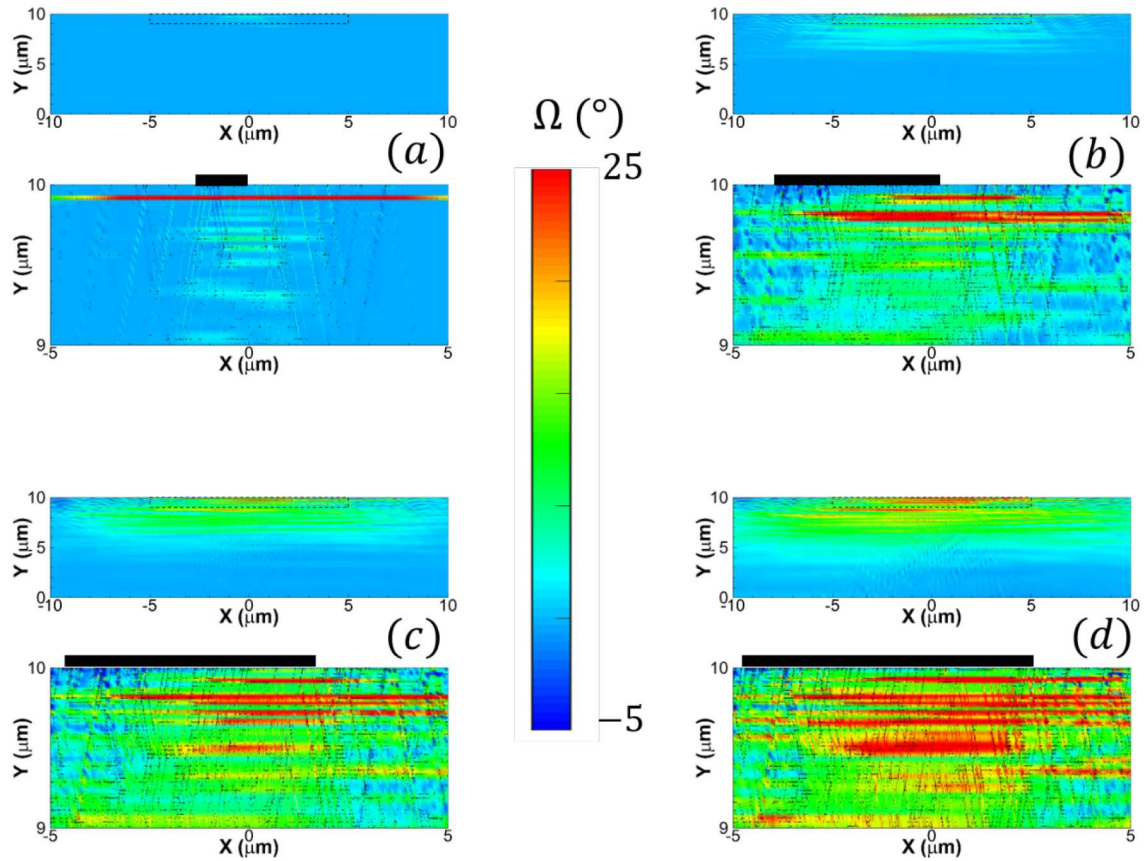
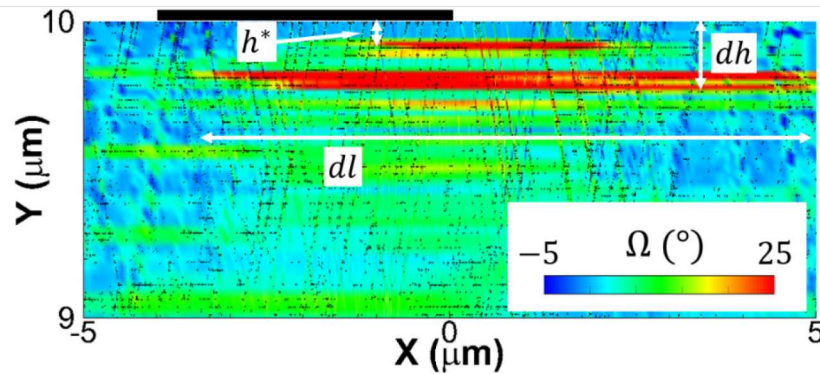


Figure 6. The contours of lattice rotation Ω and the corresponding dislocation structure (individual dislocations represented as black dots) of the sliding calculation obtained for different contact sizes. (a) $A = 1.11 \mu\text{m}$, (b) $A = 3.55 \mu\text{m}$, (c) $A = 5.52 \mu\text{m}$ and (d) $A = 8.42 \mu\text{m}$, where U is the displacement, A the contact size and δ the indentation depth. Results are shown at the instants where full sliding has been achieved for each contact size and the indenter has moved away from the initial contact area (a, b and c), or for the maximum sliding distance the calculation has reached (d). The set of lattice rotation contours illustrates the lattice rotation bands formed during sliding and the contact size effect on lattice rotation band.

Figure 7 illustrates the three characteristic dimensions of the trace lines revealed in the specimen subsurface under contact size $A = 3.55 \mu\text{m}$, which exhibits features representative of all contact sizes. The critical depth h^* indicates the distance between the surface and the boundary between the first and second trace lines, which is independent of contact size. The critical depth is predicted by the DDP model for all contact sizes as $h^* = 0.09 \mu\text{m}$, which is comparable to the experimental finding of $0.1 \mu\text{m}$ (Greiner et al., 2016). It has been verified that the tracelines predicted by the DDP simulation are not mesh or slip plane spacing dependent, are not an artefact of the

1 choice of contour levels; the mesh was fine and highly focused to the surface with a
 2 mesh size as small as $0.01\mu\text{m}$, and dislocation activity was observed between the first
 3 trace line and the contact. Both the width and height of the group of trace lines, referred
 4 to here as the lattice rotation band, labelled dl and dh , are determined by the plasticity,
 5 hence by the contact size of the preceding indentation. In the case shown here, the width
 6 of the lattice rotation band is measured as $dl = 9.5\mu\text{m}$ and the height as $dh = 6\mu\text{m}$. In
 7 the experiments the contact size was as large as $92\mu\text{m}$, much larger than in the
 8 simulations presented here (Greiner et al., 2016; Liu et al., 2018). However, as shown
 9 in **Figure 7**, dl and dh scale with the contact size, therefore it is expected that the
 10 dimensions predicted by the DDP simulations would be consistent with the
 11 experimental findings for much larger contact sizes.



12
 13 **Figure 7.** Characterization of the lattice rotation band for $U = 2.76\mu\text{m}$ and contact
 14 size $A = 3.55\mu\text{m}$. The condition of full sliding has been reached.

15 4 Discussion

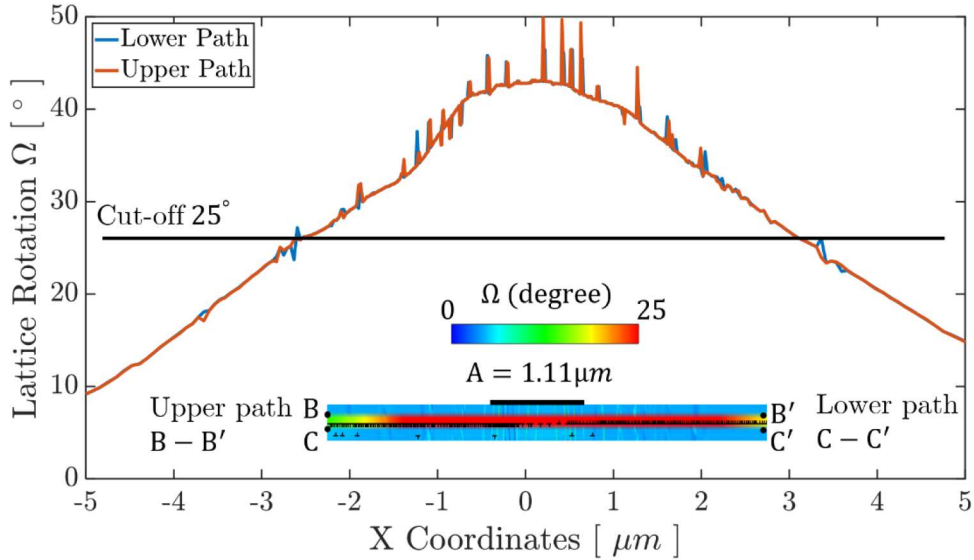
16 4.1 The origin of the lattice rotation band within the subsurface

17 It is not yet understood how the experimentally observed dislocation trace line(s)
 18 originate from the dislocation structure induced by the sliding process (Greiner et al.,
 19 2018). In the discrete dislocation plasticity calculations (**Figure 5** and **Figure 6**), the
 20 resolved shear stress is highest on the slip system parallel to the sliding direction (*i.e.*
 21 parallel to the x -axis) on the planes nearest to the surface, hence it is reasonable to

1 anticipate that dislocation activity on these slip planes is responsible for the observed
2 tracelines. As a result of the cohesive sliding boundary condition, the subsurface
3 material would like to assume a simple-shear, stack-of-cards like slip arrangement
4 (Haug et al., 2020); however compatibility with the surrounding bulk material prevents
5 that from happening perfectly, which results in a corresponding lattice rotation. The
6 mechanisms that the lattice rotation is given rise by accumulative dislocation glide and
7 crystalline slip due to geometry and boundary constraints have recently been observed
8 in other independent experimental observations including high-resolution digital image
9 correlation (HR-DIC) (Sperry et al., 2020) and high-resolution Electron backscatter
10 diffraction (HR-EBSD) (Maj et al., 2020), respectively.

11 To illustrate the origin of the dislocation traceline, the degree of rotation in the lattice
12 rotation band is plotted versus horizontal position x for contact size $A = 1.11 \mu\text{m}$
13 under a full slip condition in **Figure 9**, for both vertical extents of the band identified
14 from the lattice rotation contour plot (paths B-B' and C-C'); the width of the lattice
15 rotation band observed from the lattice rotation contour plot is dependent on the cut-off
16 value that is chosen, as shown in the figure. In the inset to **Figure 9**, it is evident that
17 dislocation dipoles pile up in queues on a single horizontal slip plane underneath the
18 contact, which are driven apart by the applied shear stress. The gradient in resolved
19 shear stress on that slip plane – it is largest at the center of the contact and decays to
20 zero far away from the cohesive sliding boundary condition – causes a ‘soft’ pile-up to
21 form. The lattice rotation at a point on the slip plane of a single dislocation dipole is
22 zero outside the dipole and a constant value anywhere within the dipole. Hence,
23 theoretically, an arrangement of concentric dipoles creates a lattice rotation profile on
24 the active slip plane that is largest at its center and decreases incrementally moving

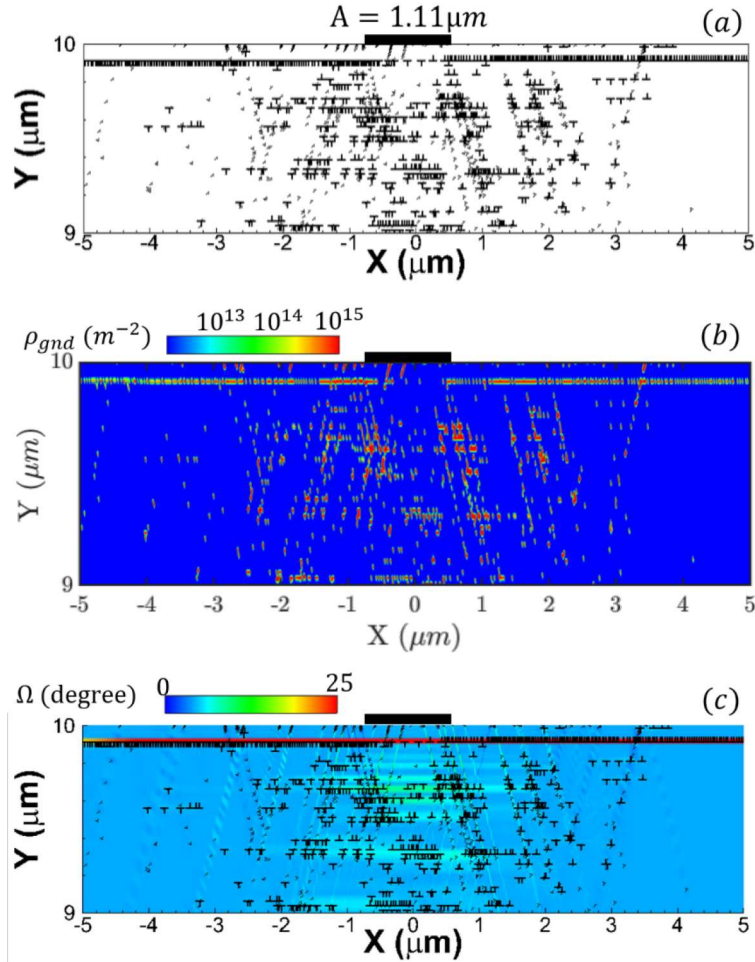
1 outward. This is what is observed in **Figure 9**, where fluctuations from the theoretical
 2 trend are caused by dislocations on other slip planes.



3
 4 **Figure 8.** Lattice rotation on a horizontal slip plane within the subsurface. Results are
 5 shown when full slip is achieved for contact size $A = 1.11 \mu\text{m}$ (see **Figure 6a**).

6 The instantaneous dislocation structure, corresponding GND density distribution and
 7 lattice rotation distribution within the specimen for a contact size $A = 1.11 \mu\text{m}$ under
 8 a full slip condition is reported in **Figure 9(a)**, **(b)** and **(c)**, respectively. Dislocations
 9 on the horizontal slip system, which are the key contributors to the lattice rotation, are
 10 identified by a dislocation symbol that is twice as large as those on the other slip systems.
 11 Localized GND density is calculated using the net open burger's vector algorithm based
 12 on the instantaneous dislocation structure (Kiener et al., 2011). A Burgers circuit size
 13 of 25nm was found to adequately resolve the GND distribution for these simulations.
 14 A strip of high GND density (**Figure 9(b)**) is identified in the same location as the
 15 lattice rotation band, which also correlates spatially with the 'soft' pile-ups of
 16 concentric dislocation dipoles on horizontal slip planes identified here as the cause of
 17 the experimental STEM observations of dislocation tracelines (Greiner et al., 2016);
 18 furthermore, the magnitude of the predicted GND density is in line with previous

1 measurements performed in sliding tests (Greiner et al., 2018; Greiner et al., 2016).
 2 Regions of low lattice rotation, particularly that of the region between the lattice
 3 rotation band and the surface, referred to here as a ‘locked-in’ layer, also correlate with
 4 low GND density as observed in the experiments.



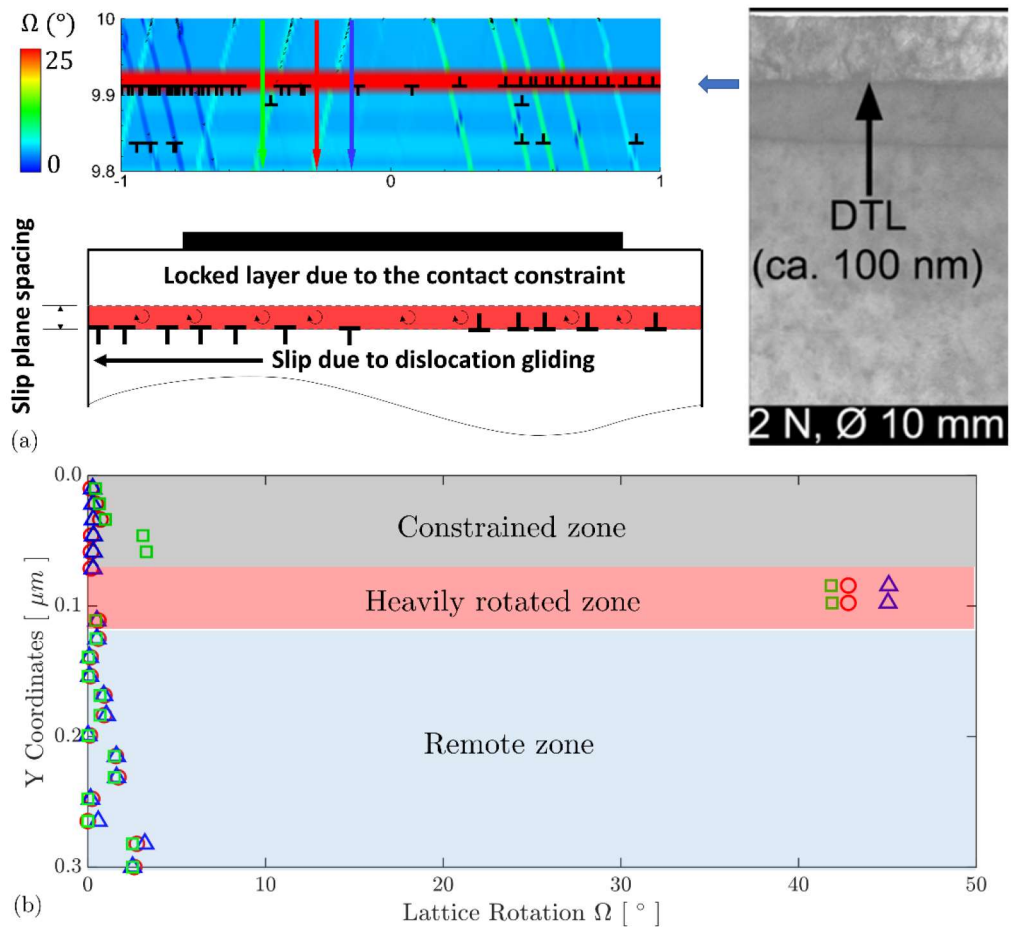
5
 6 **Figure 9.** Correlation between (a) the instantaneous distribution of dislocations, (b) the
 7 corresponding geometrically necessary dislocation (GND) density distribution and (c)
 8 lattice rotation using the discrete dislocation plasticity model. Numerical results are
 9 extracted when full sliding occurs under contact size $A = 1.11 \mu\text{m}$ (see **Figure 6a**).
 10 Dislocation symbol size is enlarged for dislocations along the horizontal slip planes.

11 **4.2 Comparison between STEM measurements and DDP simulation results**

12 In the numerical results shown in Sections 3.3 and 3.4, the emergence of the
 13 experimentally observed dislocation traceline is interpreted as a result of the formation
 14 of queues of dislocation dipoles, or soft pile-ups, on slip systems parallel to the sliding
 15 direction. In this section, we compare STEM images, which show the contrast

1 corresponding to microstructure change under sliding tests, and the lattice rotation
2 contours obtained in the simulations. A typical comparison between experiments and
3 simulations is illustrated in **Figure 10(a)**. Since the appearance of the first (uppermost)
4 traceline is common to all indenter sizes as shown in **Figure 9**, the lattice rotation is
5 post-processed from the simulation with contact size $A = 1.11 \mu\text{m}$ after full slip has
6 developed and the dislocation structure has evolved to its final configuration, as this
7 case best illustrates the mechanism responsible for the traceline and its link to lattice
8 rotation. As mentioned previously, the simulations clearly identify a region about 0.1
9 μm under the contact surface where a large number of dislocation dipoles glide parallel
10 to the surface, and a corresponding layer above it which is ‘locked-in’ and does not
11 deform appreciably. The lattice rotation along three vertical paths (defined in (a))
12 originating at the contact face are shown in **Figure 10(b)**. A significant peak indicating
13 very large lattice rotation is observed about 0.1 microns from the contact surface. This
14 peak diminishes moving from the contact center (the blue path) towards the contact
15 edge (the green path), which reflects the results in **Figure 8**. The vertical distribution
16 of lattice rotation divides the material into three layers, moving from the contact face
17 into the bulk. These are: a rotation-constrained zone, a region with significant lattice
18 rotation (due to soft pile-ups of dislocations on horizontal slip planes) and a remote
19 zone that is unaffected by the sliding. This dislocation configuration in conjunction with
20 the contact constraint induces large localised lattice rotation, interpreted physically as
21 a line (in fact, a very thin layer of material) parallel to the sliding direction across which
22 there is an abrupt change of microstructure, as observed in the experiments. This is in
23 strong agreement with the evidence provided by the companion paper that the
24 misorientation is concentrated at the DTL (see e.g. Figure 6 of Ruebeling et al. (2020)
25 and related discussion). The nature of the load and the contact size affect the behaviour

1 (and the relative lattice rotation/deformation) of the material above and below the DTL,
 2 as discussed below in more details.



3
 4 **Figure 10.** (a) Comparison between the STEM image obtained from experiments for
 5 low loads (shown on the right, zoomed-in from **Figure 6a**) and the lattice rotation and
 6 superimposed dislocation structure computed via DDP simulations (shown on the top-
 7 left, zoomed-in from Figure 9a), highlighting the dislocation activity linked to the
 8 mechanism responsible for the lattice rotation and formation of the tralceline. This is
 9 also schematically depicted at the bottom-left, showing the (b) lattice rotation
 10 distribution along three paths (defined in (a)) perpendicular to the sliding direction.
 11 Results are shown at the instant when the sliding has been initiated and dislocation
 12 motion has developed in the slip systems underneath the contact.

13 The critical depth of the 1st DTL obtained from the simulations (0.1 μm) agrees very
 14 well with the experimental findings, albeit the contact size in the two was different but
 15 this feature was shown in the simulations to be contact-size independent; the dislocation
 16 activity under the indenter is strictly controlled by the pressure and the shear traction
 17 transmitted across the interface, which is an approximate match between the

1 simulations and the values experienced by the material layer under low loads in the
2 experiments. Changing the size of the indenter changes the extent of the material
3 affected by large stresses rather than the value in the uppermost layer of the material.

4 The features shown in **Figure 10** are common to all other indentation sizes but extend
5 further into the specimens for larger indenters, with the emergence of other tracelines
6 (as also shown in the experiments) further away from the surface. The dislocation
7 activity becomes more complex when the indenter size (and hence the overall load since
8 the pressure on the indenter in the experiments is kept constant) grows due to the
9 activation of a large number of dislocations along different slip systems and slip planes.

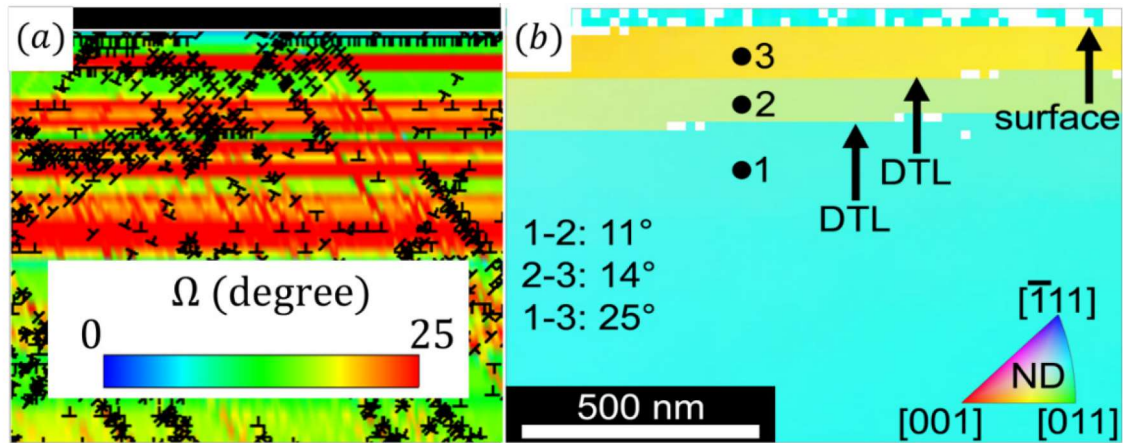
10 This usually results in progressive material rotation between tracelines (i.e. bands
11 increasing in lattice rotation between consecutive DTLs), with the largest lattice
12 rotation experienced by the plastically deformed material further away from the contact;
13 this is due to the fact that this region, which one can associate with the bulk material
14 (see **Figure 6**), is not constrained by the indenter and lattice rotation exhibits itself
15 differently in this region. This explains not only why the number of DTLs and the lattice
16 rotation increase with the size of the indenter, but also why large contact areas (typical
17 of the experiments under consideration) result in large lattice rotations recorded beneath
18 the last observable DTL, as the reach of the plastically deformed area is much deeper
19 than the area analyzed by STEM.

20 A further interesting point to discuss is that increasing the load leads to more severe
21 microstructural changes, which include increased dislocation activity and the formation
22 of small grains and re-crystallization in the tribologically affected layer. The
23 simulations in **Figure 6(d)** (largest indenter size studied here) already show very large
24 dislocation activity on different slip systems. It can be inferred that a large contact size

1 and normal load may lead to the subsequent formation of new grain boundaries that
2 have been characterized in previous experiments (Greiner et al., 2016).

3 4.3 Comparison between TKD measurements and DDP simulation results

4 The qualitative comparison between the STEM image and the lattice rotation contours
5 in **Figure 10** has shown the strong correlation between the perceived abrupt
6 microstructural changes in the experiments and the material lattice rotation under
7 sliding conditions. We turn now to quantitative measurements using Transmission
8 Kikuchi Diffraction (TKD), which have been used to determine lattice rotation in the
9 neighborhoods of the DTLs in Ruebeling et al. (2020).



10
11 **Figure 11.** The comparison between (a) lattice rotation evaluated in DDP simulations
12 with superimposed instantaneous dislocation structure and (b) lattice rotation measured
13 using the TKD pattern. Numerical results are shown for full slip and contact size $A =$
14 $95\mu\text{m}$, when dislocation motion and lattice rotation have reached their final stable
15 configuration. The simulation set-up is the closest possible scenario to replicate the one-
16 stroke sliding tests.

17 The lattice rotation within the specimen calculated using DDP and measured using
18 TKD is illustrated in **Figure 11** (a) and (b), respectively. The numerical results in
19 **Figure 11** (a) are obtained from simulations under the maximum contact size ($A =$
20 $95\mu\text{m}$) achieved in the DDP calculations, which is the closest match possible between
21 the two systems given the computational demands of DDP. The subsurface region under

1 the indenter is subjected to a similar stress state. However, the size of the indenter used
2 in the simulation is still smaller than the contact area for the equivalent experiment,
3 hence the region of material over which high stresses and strains are calculated is not
4 as deep as the equivalent region in the experimental test. The $A = 95 \mu\text{m}$ simulation is
5 nonetheless sufficient to accurately capture the lattice rotation band parallel to the
6 sliding direction underneath the contact, which is also observed in the TKD
7 experimental results shown in **Figure 11(b)**. In addition, the lattice rotation map
8 predicted by the DDP simulations exhibits several thin strips with a limited lattice
9 rotation compared to that in adjacent regions, which separate the lattice rotation band
10 from the subsurface. The separation lines are again interpreted as tracelines (*i.e.* the
11 discontinuity discussed in Section 4.1), and the depths of the first two tracelines are
12 similar to those observed in the TKD pattern map. The DDP simulations not only
13 exhibit a similar lattice rotation pattern, but the predictions also appear to be
14 quantitatively commensurate with the magnitude of misorientation measured
15 experimentally between different material strips shown in **Figure 11(b)**. For instance,
16 the lattice rotation within the most severely rotated material strip is roughly $\Omega = 30^\circ$ in
17 the DDP calculations, whereas the relative misorientation measured using TKD
18 between the surface and the region below the second traceline is $\Omega = 25^\circ$. The
19 calculated lattice rotation and misorientation measurement in the other two layers show
20 the same trend. In Section 3.4, we have shown the positive dependence of the lattice
21 rotation band dimensions on the contact size. The depth of the heavily rotated material
22 enlarges with the contact size and the lattice rotation in the simulations does not extend
23 to the full region shown in **Figure 11(b)** due to the limited contact size used for the
24 simulation. In the experiment the material below the second (lowest) DTL shows large

1 rotation deeper into the substrate (see **Figure 11b**) as the contact size is substantially
2 larger than the field of view in STEM (about one micrometre).

3 **5 Conclusion**

4 Discrete dislocation plasticity analyses have been conducted to simulate the dislocation
5 structure and localized lattice rotation under single asperity sliding, where the contact
6 between the asperity and specimen was established by a preceding sinusoidal
7 indentation. This was done to interpret the dislocation tracelines observed in
8 corresponding experiments. The following conclusions are highlighted:

9 (i) The entire sliding process up until full slip occurs is divided into three regimes by
10 sliding distance, where the two critical sliding distances demarcating these regimes are
11 identified from the shear stress and dislocation density response. Both of the critical
12 distances are found to be strongly contact size dependent.

13 (ii) The “dislocation traceline”, characterized by an abrupt contrast change observed in
14 the STEM images obtained after the first sliding stroke, is due to a highly localized
15 lattice rotation band within the material subsurface and parallel to the sliding direction,
16 which emerges with increasing sliding distance and is dependent upon the contact size.

17 The lattice rotation arises as a result of the deformation induced by the pattern of
18 concentric dislocation dipoles in conjunction with the compatibility constraint of the
19 surrounding material and the applied contact condition at the surface.

20 (iii) The critical depth from the contact to the top boundary of the horizontal lattice
21 rotation band predicted by the DDP calculations shows excellent agreement with the
22 experimental measurements. Contact size and the corresponding total normal load do
23 not affect the critical depth of the initial traceline, yet these parameters dominate the
24 width and depth of the lattice band when fully slip occurs. This finding provides

1 mechanistic insight into the damage development and subgrain formation observed in
2 tests when larger loads are applied, which have not been explicitly modelled in this
3 contribution.

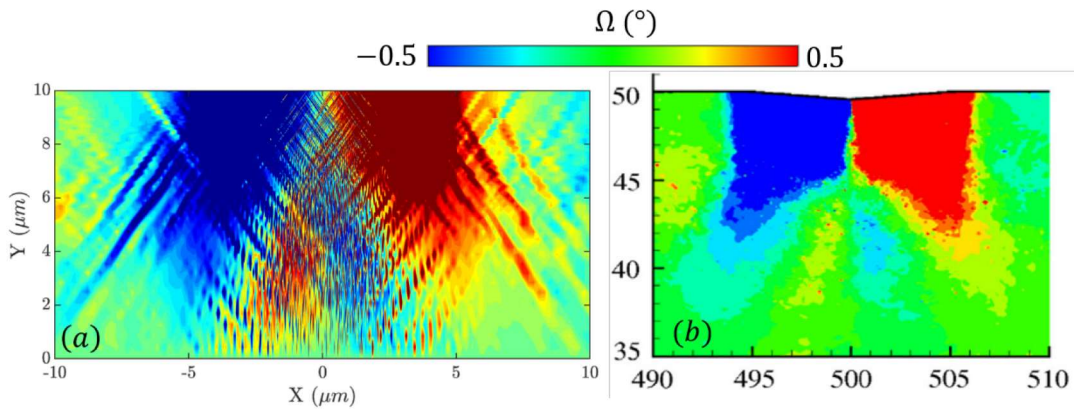
4 (iv) A very good agreement was observed between the predicted lattice rotation
5 magnitude and the experimentally measured misorientation between subsurface layers.

6 Acknowledgment

7 YX and DD would like to acknowledge funding from the EPSRC through the
8 Established Career Fellowship grant (EP/N025954/1). CG acknowledges funding the
9 European Research Council (ERC) under Grant No. 771237, TriboKey.

10 Appendix

11 Lattice rotation validation for indentation (Supplement to Section 2.3)



12
13 Figure A 1. Lattice rotation validation for indentation. Lattice rotation distribution in
14 indentation of (a) the sinusoidal indenter adopted in this research (b) a wedge-shaped
15 indenter with similar geometric characteristics studied in Zhang et al. (2014) . The result
16 is shown at the instant when the same indentation depth $\delta = 0.4 \mu\text{m}$ is imposed on both
17 indenters, respectively.

18
19

1 **References**

2 2 Akarapu, S., Zbib, H.M., Bahr, D.F., 2010. Analysis of heterogeneous deformation and
3 3 dislocation dynamics in single crystal micropillars under compression. International
4 4 Journal of Plasticity 26, 239-257 DOI: <http://dx.doi.org/10.1016/j.ijplas.2009.06.005>.

5 5 Arsenlis, A., Parks, D.M., 1999. Crystallographic aspects of geometrically-necessary
6 6 and statistically-stored dislocation density. Acta Materialia 47, 1597-1611 DOI:
7 7 [http://dx.doi.org/10.1016/S1359-6454\(99\)00020-8](http://dx.doi.org/10.1016/S1359-6454(99)00020-8).

8 8 Balint, D.S., Deshpande, V.S., Needleman, A., Van der Giessen, E., 2005. A discrete
9 9 dislocation plasticity analysis of grain-size strengthening. Mat Sci Eng a-Struct 400,
10 10 186-190 DOI: <http://dx.doi.org/10.1016/j.msea.2005.02.082>.

11 11 Balint, D.S., Deshpande, V.S., Needleman, A., Van der Giessen, E., 2006. Discrete
12 12 dislocation plasticity analysis of the wedge indentation of films. Journal of the
13 13 Mechanics and Physics of Solids 54, 2281-2303 DOI:
14 14 <http://dx.doi.org/10.1016/j.jmps.2006.07.004>.

15 15 Balint, D.S., Deshpande, V.S., Needleman, A., Van der Giessen, E., 2008. Discrete
16 16 dislocation plasticity analysis of the grain size dependence of the flow strength of
17 17 polycrystals. International Journal of Plasticity 24, 2149-2172 DOI:
18 18 <http://dx.doi.org/10.1016/j.ijplas.2007.08.005>.

19 19 Benzerga, A.A., 2008. An analysis of exhaustion hardening in micron-scale plasticity.
20 20 International Journal of Plasticity 24, 1128-1157 DOI:
21 21 <http://dx.doi.org/10.1016/j.ijplas.2007.08.010>.

22 22 Bouvier, S., Needleman, A., 2006. Effect of the number and orientation of active slip
23 23 systems on plane strain single crystal indentation. Model Simul Mater Sc 14, 1105-
24 24 1125 DOI: <http://dx.doi.org/10.1088/0965-0393/14/7/001>.

25 25 Cheng, J.H., Ghosh, S., 2015. A crystal plasticity FE model for deformation with twin
26 26 nucleation in magnesium alloys. International Journal of Plasticity 67, 148-170 DOI:
27 27 <http://dx.doi.org/10.1016/j.ijplas.2014.10.005>.

28 28 Chenje, T.W., Simbi, D.J., Navara, E., 2004. Relationship between microstructure,
29 29 hardness, impact toughness and wear performance of selected grinding media for
30 30 mineral ore milling operations. Mater Design 25, 11-18 DOI:
31 31 [http://dx.doi.org/10.1016/S0261-3069\(03\)00168-7](http://dx.doi.org/10.1016/S0261-3069(03)00168-7).

32 32 Cheong, K.S., Busso, E.P., Arsenlis, A., 2005. A study of microstructural length scale
33 33 effects on the behaviour of FCC polycrystals using strain gradient concepts.
34 34 International Journal of Plasticity 21, 1797-1814 DOI:
35 35 <http://dx.doi.org/10.1016/j.ijplas.2004.11.001>.

- 1 Counts, W.A., Braginsky, M.V., Battaile, C.C., Holm, E.A., 2008. Predicting the Hall-
2 Petch effect in fcc metals using non-local crystal plasticity. *International Journal of*
3 *Plasticity* 24, 1243-1263 DOI: <http://dx.doi.org/10.1016/j.ijplas.2007.09.008>.
- 4 Das, S., Hofmann, F., Tarleton, E., 2018. Consistent determination of geometrically
5 necessary dislocation density from simulations and experiments. *International Journal*
6 *of Plasticity* 109, 18-42 DOI: <http://dx.doi.org/10.1016/j.ijplas.2018.05.001>.
- 7 Deshpande, V.S., Balint, D.S., Needleman, A., Van der Giessen, E., 2007. Size effects
8 in single asperity frictional contacts. *Model Simul Mater Sc* 15, S97-S108 DOI:
9 <http://dx.doi.org/10.1088/0965-0393/15/1/S09>.
- 10 Deshpande, V.S., Needleman, A., Van der Giessen, E., 2004. Discrete dislocation
11 plasticity analysis of static friction. *Acta Materialia* 52, 3135-3149 DOI:
12 <http://dx.doi.org/10.1016/j.actamat.2004.03.018>.
- 13 Deshpande, V.S., Needleman, A., Van der Giessen, E., 2005. Plasticity size effects in
14 tension and compression of single crystals. *Journal of the Mechanics and Physics of*
15 *Solids* 53, 2661-2691 DOI: <http://dx.doi.org/10.1016/j.jmps.2005.07.005>.
- 16 Dunne, F.P.E., Rugg, D., Walker, A., 2007a. Lengthscale-dependent, elastically
17 anisotropic, physically-based hcp crystal plasticity: Application to cold-dwell fatigue
18 in Ti alloys. *International Journal of Plasticity* 23, 1061-1083 DOI:
19 <http://dx.doi.org/10.1016/j.ijplas.2006.10.013>.
- 20 Dunne, F.P.E., Wilkinson, A.J., Allen, R., 2007b. Experimental and computational
21 studies of low cycle fatigue crack nucleation in a polycrystal. *International Journal of*
22 *Plasticity* 23, 273-295 DOI: <http://dx.doi.org/10.1016/j.ijplas.2006.07.001>.
- 23 Greiner, C., Liu, Z.L., Schneider, R., Pastewka, L., Gumbsch, P., 2018. The origin of
24 surface microstructure evolution in sliding friction. *Scripta Mater* 153, 63-67 DOI:
25 <http://dx.doi.org/10.1016/j.scriptamat.2018.04.048>.
- 26 Greiner, C., Liu, Z.L., Strassberger, L., Gumbsch, P., 2016. Sequence of Stages in the
27 Microstructure Evolution in Copper under Mild Reciprocating Tribological Loading.
28 *Acs Applied Materials & Interfaces* 8, 15809-15819 DOI:
29 <http://dx.doi.org/10.1021/acsami.6b04035>.
- 30 Hattori, T., Kaneko, Y., Hashimoto, S., 2008. Wear-induced microstructure in Ni/Cu
31 nano-multilayers. *J Mater Sci* 43, 3923-3930 DOI: <http://dx.doi.org/10.1007/s10853-007-2372-5>.
- 33 Haug, C., Ruebeling, F., Kashiwar, A., Gumbsch, P., Kubel, C., Greiner, C., 2020. Early
34 deformation mechanisms in the shear affected region underneath a copper sliding
35 contact. *Nat Commun* 11, 839 DOI: <http://dx.doi.org/10.1038/s41467-020-14640-2>.
- 36 Hirth, J.P., Lothe, J., 1982. *Theory of dislocations*.

- 1 Hughes, D.A., Hansen, N., 2001. Graded nanostructures produced by sliding and
2 exhibiting universal behavior. *Physical Review Letters* 87, 135503 DOI:
3 <http://dx.doi.org/10.1103/PhysRevLett.87.135503>.
- 4 Johnson, K.L., 1997. Adhesion and friction between a smooth elastic spherical asperity
5 and a plane surface. *P R Soc A* 453, 163-179 DOI:
6 <http://dx.doi.org/10.1098/rspa.1997.0010>.
- 7 Karthikeyan, S., Agrawal, A., Rigney, D.A., 2009. Molecular dynamics simulations of
8 sliding in an Fe-Cu tribopair system. *Wear* 267, 1166-1176 DOI:
9 <http://dx.doi.org/10.1016/j.wear.2009.01.032>.
- 10 Kiener, D., Guruprasad, P.J., Keralavarma, S.M., Dehm, G., Benzerga, A.A., 2011.
11 Work hardening in micropillar compression: In situ experiments and modeling. *Acta*
12 *Materialia* 59, 3825-3840 DOI: <http://dx.doi.org/10.1016/j.actamat.2011.03.003>.
- 13 Kuksenko, V., Roberts, S., Tarleton, E., 2019. The hardness and modulus of
14 polycrystalline beryllium from nano-indentation. *International Journal of Plasticity* 116,
15 62-80 DOI: <http://dx.doi.org/https://doi.org/10.1016/j.ijplas.2018.12.008>.
- 16 Kysar, J.W., Saito, Y., Oztop, M.S., Lee, D., Huh, W.T., 2010. Experimental lower
17 bounds on geometrically necessary dislocation density. *International Journal of*
18 *Plasticity* 26, 1097-1123 DOI: <http://dx.doi.org/10.1016/j.ijplas.2010.03.009>.
- 19 Lewandowski, M.J., Stupkiewicz, S., 2018. Size effects in wedge indentation predicted
20 by a gradient-enhanced crystal-plasticity model. *International Journal of Plasticity* 109,
21 54-78 DOI: <http://dx.doi.org/https://doi.org/10.1016/j.ijplas.2018.05.008>.
- 22 Liu, Z.L., Patzig, C., Selle, S., Hoche, T., Gumbsch, P., Greiner, C., 2018. Stages in the
23 tribologically-induced oxidation of high-purity copper. *Scripta Mater* 153, 114-117
24 DOI: <http://dx.doi.org/10.1016/j.scriptamat.2018.05.008>.
- 25 Maj, M., Nowak, M., Musial, S., Plocinski, T., 2020. Experimental analysis of material,
26 lattice and plastic rotation during deformation of aluminium multicrystal. *Mat Sci Eng*
27 *a-Struct* 790, 139725 DOI: <http://dx.doi.org/10.1016/j.msea.2020.139725>.
- 28 Meissonnier, F.T., Busso, E.P., O'Dowd, N.P., 2001. Finite element implementation of
29 a generalised non-local rate-dependent crystallographic formulation for finite strains.
30 *International Journal of Plasticity* 17, 601-640 DOI: [http://dx.doi.org/10.1016/S0749-6419\(00\)00064-4](http://dx.doi.org/10.1016/S0749-6419(00)00064-4).
- 31
32
33
34 Nix, W.D., Gao, H.J., 1998. Indentation size effects in crystalline materials: A law for
35 strain gradient plasticity. *Journal of the Mechanics and Physics of Solids* 46, 411-425
36 DOI: [http://dx.doi.org/10.1016/S0022-5096\(97\)00086-0](http://dx.doi.org/10.1016/S0022-5096(97)00086-0).

- 1 Pastewka, L., Moser, S., Gumbsch, P., Moseler, M., 2011. Anisotropic mechanical
2 amorphization drives wear in diamond. *Nature Materials* 10, 34-38 DOI:
3 <http://dx.doi.org/10.1038/Nmat2902>.
- 4 Pharr, G.M., Herbert, E.G., Gao, Y.F., 2010. The Indentation Size Effect: A Critical
5 Examination of Experimental Observations and Mechanistic Interpretations. *Annu Rev*
6 *Mater Res* 40, 271-292 DOI: <http://dx.doi.org/10.1146/annurev-matsci-070909-104456>.
- 7 Po, G., Huang, Y., Ghoniem, N., 2019. A continuum dislocation-based model of wedge
8 microindentation of single crystals. *International Journal of Plasticity* 114, 72-86 DOI:
9 <http://dx.doi.org/https://doi.org/10.1016/j.ijplas.2018.10.008>.
- 10 Prastiti, N.G., Xu, Y.L., Balint, D.S., Dunne, F.P.E., 2020. Discrete dislocation, crystal
11 plasticity and experimental studies of fatigue crack nucleation in single-crystal nickel.
12 *International Journal of Plasticity* 126 DOI:
13 <http://dx.doi.org/10.1016/j.ijplas.2019.10.003>.
- 14 Qu, S., Huang, Y., Pharr, G.M., Hwang, K.C., 2006. The indentation size effect in the
15 spherical indentation of iridium: A study via the conventional theory of mechanism-
16 based strain gradient plasticity. *International Journal of Plasticity* 22, 1265-1286 DOI:
17 <http://dx.doi.org/10.1016/j.ijplas.2005.07.008>.
- 18 Rigney, D.A., Glaeser, W.A., 1978. Significance of near-Surface Microstructure in
19 Wear Process. *Wear* 46, 241-250 DOI: [http://dx.doi.org/10.1016/0043-1648\(78\)90125-](http://dx.doi.org/10.1016/0043-1648(78)90125-4)
20 [4](http://dx.doi.org/10.1016/0043-1648(78)90125-4).
- 21 Rigney, D.A., Hirth, J.P., 1979. Plastic-Deformation and Sliding Friction of Metals.
22 *Wear* 53, 345-370 DOI: [http://dx.doi.org/10.1016/0043-1648\(79\)90087-5](http://dx.doi.org/10.1016/0043-1648(79)90087-5).
- 23 Ruebeling, F., Xu, Y., Richter, G., Dini, D., Gumbsch, P., Greiner, C., 2020. How
24 normal load and counter body size influence the initiation of microstructural
25 discontinuities in copper during sliding. *ACS Applied Materials and Interfaces* (under
26 review).
- 27 Saraev, D., Miller, R.E., 2006. Atomic-scale simulations of nanoindentation-induced
28 plasticity in copper crystals with nanometer-sized nickel coatings. *Acta Materialia* 54,
29 33-45 DOI: <http://dx.doi.org/10.1016/j.actamat.2005.08.030>.
- 30 Song, H., Deshpande, V.S., Van der Giessen, E., 2016. Discrete dislocation plasticity
31 analysis of loading rate-dependent static friction. *P Roy Soc a-Math Phy* 472, 20150877
32 DOI: <http://dx.doi.org/10.1098/rspa.2015.0877>.
- 33 Sperry, R., Harte, A., da Fonseca, J.Q., Homer, E.R., Wagoner, R.H., Fullwood, D.T.,
34 2020. Slip band characteristics in the presence of grain boundaries in nickel-based
35 superalloy. *Acta Materialia* 193, 229-238 DOI:
36 <http://dx.doi.org/10.1016/j.actamat.2020.04.037>.

1 Stoyanov, P., Romero, P.A., Merz, R., Kopnarski, M., Stricker, M., Stemmer, P.,
2 Dienwiebel, M., Moseler, M., 2014. Nano scale sliding friction phenomena at the
3 interface of diamond-like carbon and tungsten. *Acta Materialia* 67, 395-408 DOI:
4 <http://dx.doi.org/10.1016/j.actamat.2013.12.029>.

5
6 Tarleton, E., Balint, D.S., Gong, J., Wilkinson, A.J., 2015. A discrete dislocation
7 plasticity study of the micro-cantilever size effect. *Acta Materialia* 88, 271-282 DOI:
8 <http://dx.doi.org/10.1016/j.actamat.2015.01.030>.

9
10 Van der Giessen, E., Needleman, A., 1995. Discrete Dislocation Plasticity - a Simple
11 Planar Model. *Model Simul Mater Sc* 3, 689-735.

12
13 Widjaja, A., Van der Giessen, E., Deshpande, V.S., Needleman, A., 2007a. Contact
14 area and size effects in discrete dislocation modeling of wedge indentation. *J Mater Res*
15 22, 655-663 DOI: <http://dx.doi.org/10.1557/Jmr.2007.0090>.

16
17 Widjaja, A., Van der Giessen, E., Needleman, A., 2007b. Discrete dislocation analysis
18 of the wedge indentation of polycrystals. *Acta Materialia* 55, 6408-6415 DOI:
19 <http://dx.doi.org/10.1016/j.actamat.2007.07.053>.

20
21 Xu, Y., Balint, D.S., Dini, D., 2016. A method of coupling discrete dislocation plasticity
22 to the crystal plasticity finite element method. *Model Simul Mater Sc* 24, 045007 DOI:
23 <http://dx.doi.org/10.1088/0965-0393/24/4/045007>.

24
25 Xu, Y., Balint, D.S., Dini, D., 2019. A new hardness formula incorporating the effect
26 of source density on indentation response: A discrete dislocation plasticity analysis.
27 *Surf Coat Tech* 374, 763-773 DOI: <http://dx.doi.org/10.1016/j.surfcoat.2019.06.045>.

28
29 Xu, Y., Fox, K., Rugg, D., Dunne, F.P.E., 2020. Cyclic plasticity and thermomechanical
30 alleviation in titanium alloys. *International Journal of Plasticity* 134, 102753 DOI:
31 <http://dx.doi.org/10.1016/j.ijplas.2020.102753>.

32
33 Zhang, M., Neu, R.W., McDowell, D.L., 2009. Microstructure-sensitive modeling:
34 Application to fretting contacts. *Int J Fatigue* 31, 1397-1406 DOI:
35 <http://dx.doi.org/10.1016/j.ijfatigue.2009.03.023>.

36
37 Zhang, Y.H., Gao, Y.F., Nicola, L., 2014. Lattice rotation caused by wedge indentation
38 of a single crystal: Dislocation dynamics compared to crystal plasticity simulations.
39 *Journal of the Mechanics and Physics of Solids* 68, 267-279 DOI:
40 <http://dx.doi.org/10.1016/j.jmps.2014.04.006>.